

Periodic activity from a fast radio burst source

The CHIME/FRB Collaboration, Amiri, M.¹, Andersen, B. C.^{2,3}, Bandura, K. M.^{4,5}, Bhardwaj, M.^{2,3}, Boyle, P. J.^{2,3}, Brar, C.^{2,3}, Chawla, P.^{2,3}, Chen, T.⁶, Cliche, J. F.^{2,3}, Cubranic, D.¹, Deng, M.¹, Denman, N. T.⁷, Dobbs, M.^{2,3}, Dong, F. Q.¹, Fandino, M.¹, Fonseca, E.^{2,3}, Gaensler, B. M.^{8,9}, Giri, U.^{10,11}, Good, D. C.¹, Halpern, M.¹, Hessels, J. W. T.^{12,13}, Hill, A. S.^{14,15}, Höfer, C.¹, Josephy, A.^{2,3}, Kania, J. W.¹⁶, Karuppusamy, R.¹⁷, Kaspi, V. M.^{2,3}, Keimpema, A.¹⁸, Kirsten, F.¹⁹, Landecker, T. L.¹⁵, Lang, D. A.^{10,11}, Leung, C.^{6,20}, Li, D. Z.^{21,22,17,8*}, Lin, H.-H.^{21,17}, Marcote, B.¹⁸, Masui, K. W.^{6,20}, Mckinven, R.^{8,9}, Mena-Parra, J.⁶, Merryfield, M.^{2,3}, Michilli, D.^{2,3}, Milutinovic, N.^{1,15}, Mirhosseini, A.¹, Naidu, A.^{2,3}, Newburgh, L. B.²³, Ng, C.⁸, Nimmo, K.^{12,13}, Paragi, Z.¹⁸, Patel, C.^{8,2,3}, Pen, U.-L.^{21,8,24,10,17}, Pinsonneault-Marotte, T.¹, Pleunis, Z.^{2,3}, Rafiei-Ravandi, M.¹⁰, Rahman, M.⁸, Ransom, S. M.²⁵, Renard, A.⁸, Sanghavi, P.^{4,5}, Scholz, P.^{8,15}, Shaw, J. R.¹, Shin, K.^{6,20}, Siegel, S. R.^{2,3}, Singh, S.^{2,3}, Smegal, R. J.¹, Smith, K. M.¹⁰, Stairs, I. H.¹, Tendulkar, S. P.^{2,3}, Tretyakov, I.^{8,22}, Vanderlinde, K.^{8,9}, Wang, H.^{6,20}, Wang, X.²⁶, Wulf, D.^{2,3}, Yadav, P.¹, Zwaniga, A. V.^{2,3}

* Corresponding Author

¹Department of Physics and Astronomy, University of British Columbia, 6224 Agricultural Road, Vancouver, BC V6T 1Z1, Canada

²Department of Physics, McGill University, 3600 rue University, Montréal, QC H3A 2T8, Canada

³McGill Space Institute, McGill University, 3550 rue University, Montréal, QC H3A 2A7, Canada

⁴CSEE, West Virginia University, Morgantown, WV 26505, USA

⁵Center for Gravitational Waves and Cosmology, West Virginia University, Morgantown, WV 26505, USA

⁶MIT Kavli Institute for Astrophysics and Space Research, Massachusetts Institute of Technology, 77 Massachusetts Ave, Cambridge, MA 02139, USA

⁷Central Development Laboratory, National Radio Astronomy Observatory, 1180 Boxwood Estate Road, Charlottesville VA 22903, USA

⁸Dunlap Institute for Astronomy & Astrophysics, University of Toronto, 50 St. George Street, Toronto, ON M5S 3H4, Canada

⁹David A. Dunlap Department of Astronomy & Astrophysics, University of Toronto, 50 St. George Street, Toronto, ON M5S 3H4, Canada

¹⁰Perimeter Institute for Theoretical Physics, 31 Caroline Street N, Waterloo ON N2L 2Y5, Canada

¹¹Department of Physics and Astronomy, University of Waterloo, Waterloo, ON N2L 3G1, Canada

¹²ASTRON, Netherlands Institute for Radio Astronomy, Oude Hoogeveensedijk 4, 7991 PD Dwingeloo, The Netherlands

¹³Anton Pannekoek Institute for Astronomy, University of Amsterdam, Science Park 904, 1098 XH Amsterdam, The Netherlands

¹⁴Department of Computer Science, Math, Physics, and Statistics, University of British Columbia, 3187 University Way, Kelowna, BC V1V 1V7, Canada

¹⁵Dominion Radio Astrophysical Observatory, Herzberg Research Centre for Astronomy and Astrophysics, National Research Council Canada, PO Box 248, Penticton, BC V2A 6J9, Canada

¹⁶Department of Physics and Astronomy, West Virginia University, Morgantown, WV 26505, USA

¹⁷Max Planck Institute for Radio Astronomy, Auf dem Huegel 69, Bonn, 53121, Germany

¹⁸Joint Institute for VLBI ERIC (JIVE), Oude Hoogeveensedijk 4, 7991 PD Dwingeloo, The Netherlands

¹⁹Department of Space, Earth and Environment, Chalmers University of Technology, Onsala Space Observatory, 439 92, Onsala, Sweden

Fast radio bursts (FRBs) are bright, millisecond-duration radio transients originating from extragalactic distances¹. Their origin is unknown. Some FRB sources emit repeat bursts, ruling out cataclysmic origins for those events²⁻⁴. Despite searches for periodicity in repeat burst arrival times on time scales from milliseconds to many days^{2,5-7}, these bursts have hitherto been observed to appear sporadically, and though clustered⁸, without a regular pattern. Here we report the detection of a 16.35 ± 0.18 day periodicity from a repeating FRB 180916.J0158+65 detected by the Canadian Hydrogen Intensity Mapping Experiment Fast Radio Burst Project (CHIME/FRB)^{4,9}. In 28 bursts recorded from 16th September 2018 through 30th October 2019, we find that bursts arrive in a 4.0-day phase window, with some cycles showing no bursts, and some showing multiple bursts, within CHIME’s limited daily exposure. Our results suggest a mechanism for periodic modulation either of the burst emission itself, or through external amplification or absorption, and disfavour models invoking purely sporadic processes.

Last year the CHIME/FRB collaboration reported the discovery of eight new repeating FRB sources⁴, including FRB 180916.J0158+65, which was recently localized to a star-forming region in a nearby massive spiral galaxy at redshift 0.0337 ± 0.0002 ¹⁰. From September 2018 to November 2019, CHIME/FRB has detected a total of 28 bursts from FRB 180916.J0158+65, which remains the most active source from this recent CHIME/FRB repeater sample. The barycentric arrival times for the 28 bursts (including those has been published before) from FRB 180916.J0158+65, corrected for delays from pulse dispersion, are listed in Extended Data Table 1.

To search for periodicity, the burst arrival times (spanning a 400-day time range) were folded with different periods from 1.57 to 62.8 days (see Methods), with a Pearson’s χ^2 test applied to each resulting profile with 8 phase bins¹¹. A reduced $\chi^2 \gg 1$ with respect to a uniform distribution indicates a periodicity unlikely to arise by chance. Furthermore, to account for the possible non-Poissonian statistics of the bursts¹², we have applied the search with different weighting schemes that consider clustered bursts of different time range to be correlated events (see Methods).

Searches with different weightings return periodograms of similar shape and have the same primary peak with significance varying between $3.5 - 8\sigma$. As an example, the reduced χ^2 versus period using a weighting that counts only active days instead of individual events is shown in Figure 1a. A distinct peak is detected at 16.35 ± 0.18 days, with

²⁰Department of Physics, Massachusetts Institute of Technology, 77 Massachusetts Ave, Cambridge, MA 02139, USA

²¹Canadian Institute for Theoretical Astrophysics, 60 St. George Street, Toronto, ON M5S 3H8, Canada

²²Department of Physics, University of Toronto, 60 St. George Street, Toronto, ON M5S 1A7, Canada

²³Department of Physics, Yale University, New Haven, CT 06520, USA

²⁴Canadian Institute for Advanced Research, CIFAR Program in Gravitation and Cosmology, Toronto, ON M5G 1Z8, Canada

²⁵National Radio Astronomy Observatory, 520 Edgemont Road, Charlottesville, VA 22903, USA

²⁶School of Physics and Astronomy, Sun Yat-sen University, 2 Daxue Road, Zhuhai, China

a probability of chance occurrence $\sim 10^{-7}$ (equivalent to 5σ), accounting for the number of independent periods searched. The other χ^2 peaks correspond to harmonics and sub-harmonics of the period, with the one at 32.7 days being the next most prominent. As a check, the same procedure was run on two types of control samples (1) a mock data set, consisting of burst arrival times randomly sampled according to the daily exposure of FRB 180916.J0158+65 with the full width half maximum (FWHM) of the telescopes synthesize beams at 600 MHz (Figure 1b) and (2) randomly selected pulses from Galactic radio pulsars of similar declination detected by CHIME/FRB (Figure 1c) which have the same limited daily exposure and long-term sensitivity changes as the data for FRB 180916.J0158+65. The 16.35-day periodicity is absent in the control samples, and with 10^6 sets of control samples of each type, no other periods have reached the level of significance of the 16.35-day period for FRB 180916.J0158+65 by chance coincidence.

Alternative search methods, such as folding the events and evaluating the resulting profiles using the H-test¹³, and discrete Fourier transform searches with incoherent harmonic summing¹⁴, also return the 16.35-day period, with nominal significances between 4 and 11σ under various assumptions (see Methods). Figure 2 shows the arrival times of the bursts from FRB 180916.J0158+65 from 28th August 2018 to 30th September 2019, together with the daily exposure to the source and instrument sensitivity. The instrument was operating for the majority of this time interval with nominal sensitivity; however, the bursts are seen to be detected only in a narrow interval at the reported periodicity. We conclude that this is the first detected periodicity of any kind in an FRB source.

In addition to the CHIME/FRB detections, FRB 180916.J0158+65 was detected by the European Very-long-baseline-interferometry Network (EVN) during 3.5 hours of exposure on 19th June 2019 at a central frequency of 1.7 GHz¹⁰. The EVN arrival times appear at the very leading edge of the active phase determined from analysis of CHIME/FRB timing data at lower frequencies of 400–800 MHz (Figures 2 and 3). On the other hand, during a predicted epoch of peak activity (29th October 2019 and 30th October 2019), we observed towards the direction of FRB 180916.J0158+65 for 17.6 h using the 100-m Effelsberg telescope at 1.4 GHz (see Methods). In the search, we did not detect any bursts above a fluence limit of 0.17 Jy ms (for bursts with widths of 1 ms). These observations were contemporaneous with two CHIME/FRB detected bursts from FRB 180916.J0158+65. The detection of bursts with CHIME/FRB with only ~ 12 min daily exposure and simultaneous non-detection with Effelsberg with 17.6 h exposure in two peak active days is suggestive of a frequency dependence to the burst activity. Future multi-frequency radio observations of FRB 180916.J0158+65 will aid in understanding the relationship between burst activity and emission frequency.

The burst activity is not constant within the active phase (Figure 3c), causing the burst-rate estimate to depend strongly on the definition of the active phase. The detection rate estimated with the CHIME/FRB system in a ± 0.8 -day interval (standard deviation in the phases derived by folding burst arrival times) around each epoch of activity is $1.8^{+1.3}_{-0.9}$ bursts hour⁻¹ above a fluence threshold of 5.2 Jy ms. The rate is estimated from 12 of the 28 detections with the associated 95% confidence limits based on Poisson statistics

(see Methods). For a ± 2.6 -day interval which includes the arrival times of all bursts, we find the detection rate to be $1.0^{+0.5}_{-0.4}$ bursts hour⁻¹, based on 19 of the 28 detections. (Although all bursts are emitted in a 4.0-day phase window, the above interval is larger as it assumes the activity window to be symmetric about the mean phase of burst arrival times.) The 95% confidence upper limit on the detection rate during inactive phases with non-zero exposure is 0.07 bursts per hour above a fluence threshold of 5.1 Jy ms. Fluence thresholds are complete to the 90% confidence level.

Figure 3 shows the burst fluence and DM as a function of phase. The phase is computed by folding burst arrival times at a period of 16.35 days with MJD 58369.30 referenced as phase 0. In this definition, phase 0.5 corresponds to the mean of the folded arrival times. There is no apparent trend of burst fluence in the 400–800 MHz band with phase. The best-fit DMs of four CHIME/FRB bursts with high time resolution data (marked red), as well as the DM of the brightest burst detected by the EVN¹⁰, which is accurately determined due to the bursts narrowness, are consistent with each other, constraining changes in DM to be < 0.1 pc cm⁻³. These bursts are detected over a time span of ~ 176 days, which strongly constrains any potential DM variation within this time period. The DMs of the other bursts, although possibly subject to important biases (see Methods), disfavour DM changes greater than 2 pc cm⁻³ over the full 400-day span of the events. In summary, there is no obvious phase- or time-related change in DM in the current data.

Bursts from FRB 180916.J0158+65 and other repeating FRB sources display complex morphological features: they tend to exhibit 100–200 MHz bandwidth at different central frequencies, with temporal widths of a few ms to tens of ms; some exhibit downward-drifting sub-bursts at a few to tens of MHz ms⁻¹ in the CHIME band⁴, up to almost a GHz ms⁻¹ at 6.5 GHz in the case of FRB 121102^{15,16}. We observe no trend in burst temporal width or bandwidth for burst detections by CHIME/FRB thus far, neither as a function of time nor phase. Moreover, drifting sub-bursts appear to occur at all phases. In fact, when dedispersed to the average best-fit DM from high-resolution baseband data (as in Extended Data Figure 2) nearly all bursts seem to exhibit downward-drifting sub-bursts.

The discovery of a 16.35-day periodicity in a repeating FRB source is an important clue to the nature of this object. One possible explanation is orbital motion, with either a stellar or compact-object companion. Given the source’s location¹⁰ in the outskirts of a massive spiral galaxy, a supermassive black hole companion seems unlikely, although lower-mass black holes are viable. Binary systems permit measurements of system properties including the presence of a companion wind and the matter inhomogeneities in the environment of the system via DM and/or rotation measure variations. In case the bursts scintillate even the inclination of the binary orbit and the companion mass can be determined^{17–19}. The single constraint on the orbital period still allows several orders of magnitude range in companion mass amongst known stellar-mass compact object binaries: from so-called “black widow” binary systems, consisting of a low-mass star and a powerful millisecond pulsar whose wind ablates the companion²⁰ (albeit typically with few-hour orbital periods), to massive O/B stars with highly eccentric companion

pulsar orbits ^{21–23}. In Galactic binaries composed of a massive star and pulsar, bright X-ray and γ -ray emission can be observed²⁴, and if in the future detected in this system, would be a strong diagnostic, though the much larger distance to FRB 180916.J0158+65 (~ 149 Mpc¹⁰) will make a detection challenging with current instruments. The narrow duty cycle for bursting in the FRB 180916.J0158+65 system could be related to eccentricity: a stellar companion could stimulate emission through a physical wind^{25,26}, or a black hole through magnetic/tidal interactions²⁷. Propagation effects, including plasma eclipse and magnification, could also play a role; FRBs could be generated if, for example, giant radio pulses from an energetic neutron star are strongly lensed/eclipsed by the companion wind/disk near periastron^{20,21,28,29}. The strong chromacity of the FRB spectrum resembles pulsar plasma lensing^{28,30}. However, a challenge for this picture is the preference of downward-drifting frequency structure in observed bursts (see Fig. 2). This would require a time-motion asymmetry, for example shocks in a companion wind.

Isolated compact object scenarios may be consistent with the data, but also present challenges. One popular model to explain repeating FRBs invokes a magnetar central engine ^{31–33}. A periodicity could arise from the rotation of such a star. However, known Galactic magnetars³⁴ have rotation periods < 12 s. One young 6.67-hr X-ray pulsar has been argued to be a magnetar^{35,36}, with torque from a disk of material having spun it down. However, simulations of such “fall-back disks” ³⁷ suggest it is difficult to produce periodicities of several hours, let alone several weeks. A handful of known radio pulsars show intermittent, quasi-periodic emission intervals having periods of several days, and which are known to be magnetospheric in origin³⁸ (though otherwise poorly understood). However, those sources’ radio luminosities are at least nine orders of magnitude lower than in this, and all other, FRB sources. A precessing, isolated spinning pulsar could modulate the visibility. Long-lived precession in isolated neutron stars was thought impossible because of rapid damping due to superfluid vortex line pinning in the stellar interior ³⁹. More recent work ^{40–42} incorporates modifications to the superfluid properties and may allow for precession. If the source were precessing, the bursts would likely be emerging from a fixed region on the star, likely a magnetic pole, and the ~ 0.2 burst active phase would suggest either a small viewing angle or a large polar region, possibilities that may be distinguishable using observations of the variation of the position angle of linearly polarized emission.

Future observations, both intensity and polarimetric, and at all wavebands, could distinguish among models and are strongly encouraged, as are searches for periodicities in other repeaters, to see if the phenomenon is generic.

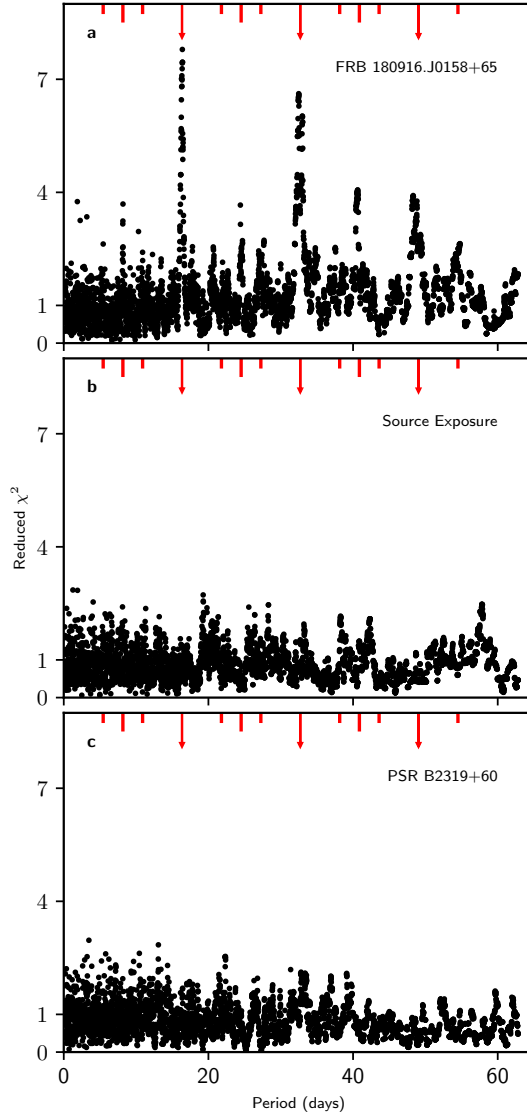


Figure 1: **Periodograms of FRB 180916.J0158+65 and control samples.** **a:** the reduced χ^2 with respect to a uniform distribution of burst arrival times for different folding periods for FRB 180916.J0158+65 detected by CHIME/FRB. Only samples separated by a sidereal day are considered independent in this approach. Details of the calculation of χ^2 and other approaches are presented in Methods. **b:** the periodogram of mock burst arrival times randomly sampled according to the daily exposure to FRB 180916.J0158+65 within the FWHM of the telescopes synthesized beams at 600 MHz. **c:** the periodogram of randomly selected pulses of Galactic radio pulsar B2319+60 detected by the same instrument and software. The arrows indicate the first 3 subharmonics of the 16.35-day periodicity, while the vertical lines mark the harmonics of 1/2 period (longer lines) and 1/3 period (shorter lines).

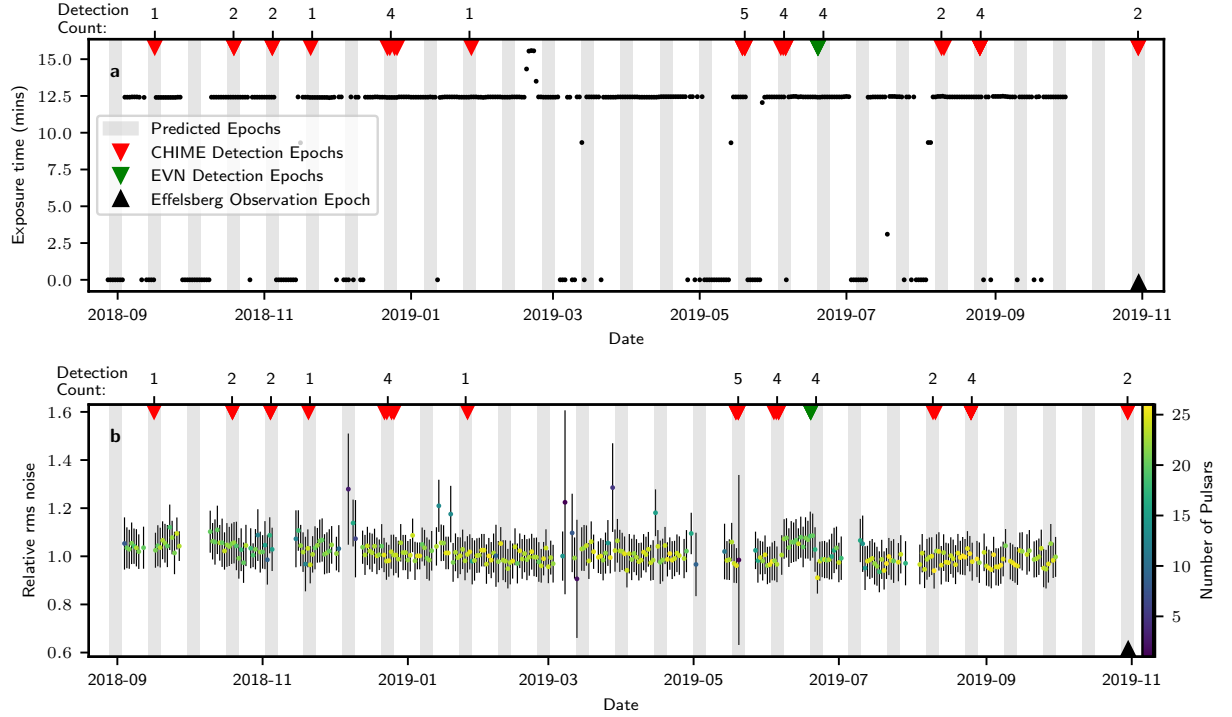


Figure 2: **a**: Timeline of CHIME/FRB’s daily exposure to FRB 180916.J0158+65 within the FWHM of the synthesized beams at 600 MHz, shown in black. Downward triangle markers indicate arrival times for detections with CHIME/FRB or EVN with the number of detections in each active phase indicated above these markers while the upward triangle marker indicates the epoch of non-detection of the source by the Effelsberg telescope. The grey shaded regions show a ± 2.6 -day interval around estimated epochs of source activity. The exposure for October 2019 is not plotted due to an upgrade of the software (see Methods). **b**: The variation in the daily relative RMS noise at the position of FRB 180916.J0158+65, depicted as coloured points with uncertainties, measured using a collection of pulsars detected by CHIME/FRB. Non-detection of the source at some, but not all, of the predicted epochs are likely due to zero exposure to the source or low sensitivity at that epoch. There is clearly significant exposure and nominal sensitivity to the source well outside the regions of observed activity.

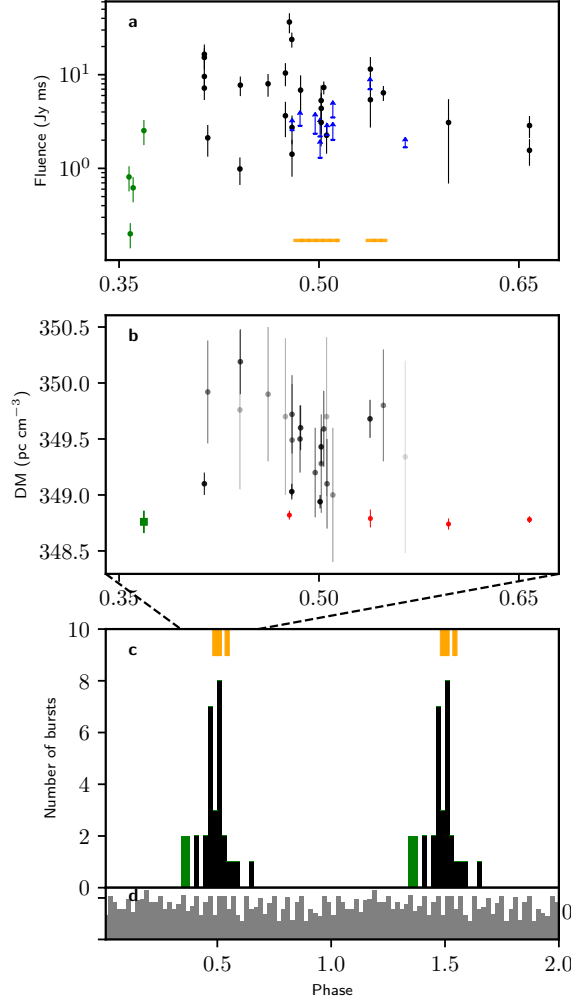


Figure 3: **Burst properties against phase.** FRB 180916.J0158+65 bursts folded at the 16.35-day period with MJD 58369.30 referenced as phase 0. Properties of 1.7 GHz EVN detection are in green; constraints from 1.4 GHz Effelsberg non-detection are in orange. The rests are from CHIME/FRB observation. **a:** Fluence versus phase. Blue arrows indicate lower bounds derived from CHIME detection; orange lines are the fluence threshold for 1 ms bursts for the search in Effelsberg data. **b:** DM versus phase. DMs derived from high-resolution baseband data from CHIME/FRB are in red. DMs from CHIME/FRB intensity data are in black, which undergo potential biases(see Methods). Data points with larger errors are assigned with higher transparency. **c:** Number of bursts at each phase. Orange blocks are the corresponding phases of the Effelsberg non-detection. **d:** Relative exposure time of different phase bins to FRB 180916.J0158+65 within the FWHM of the CHIME synthesized beams at 600 MHz.

Methods

Burst characterization: Burst DMs and models of dynamic spectra were determined in a manner similar to that used for earlier detections of the source³. In summary, bursts were dedispersed to a fiducial $DM = 349.75 \text{ pc cm}^{-3}$ and their DMs were subsequently optimized to maximize structure by calculating the phase coherence of emission in all frequency channels with the `DM_phase` package¹ (Seymour et al. in prep.) over a range of trial DMs. The alignment of sub-bursts in burst dynamic spectra was verified by eye and best-fit values are listed in Extended Data Table 1.

In addition, we fit structure-optimizing DMs using the same method for four FRB 180916.J0158+65 bursts for which complex voltage (baseband) data were saved to disk: the 181225 and 181226 bursts presented previously⁴, and the 190604 burst and second 190605 burst presented in this work. The baseband system has a $2.56\text{-}\mu\text{s}$ time resolution and 0.390625-MHz frequency resolution, but we downsampled the data in time to 40.96, 40.96, 20.48 and $81.92 \mu\text{s}$, for the four bursts respectively, to optimize S/N and resolution. We find DMs 348.78 ± 0.02 , 348.82 ± 0.02 , 348.82 ± 0.05 and $348.86 \pm 0.05 \text{ pc cm}^{-3}$, respectively, align the sub-structures in the four bursts best. We note that DMs measured from CHIME/FRB intensity data, which have 0.98304-ms time resolution, are biased high if a burst is comprised of unresolved downward-drifting sub-bursts that only become obvious at higher time resolution. As the DMs fitted at high time resolution are all consistent with one average $DM = 348.82 \text{ pc cm}^{-3}$, which is also consistent with the DM of the brightest burst detected by the EVN¹⁰, we use that value to dedisperse intensity data for visualization of the millisecond-resolution data.

Dynamic spectra for the four bursts for which the baseband data (at a time resolution of few tens of μs) were analyzed are shown in Extended Data Figure 1 and dynamic spectra of the intensity data (at \sim millisecond time resolution) for the 16 new bursts presented in this work are shown in Extended Data Figure 2.

Single- or multi-component models of dynamic spectra were fit to millisecond-resolution total-intensity data acquired for each burst using a least-squares algorithm^{3,4,16,43}. We applied two-dimensional models of spectra that consisted of Gaussian temporal shapes and either Gaussian or weighted power-law spectral energy distributions. Due to the complex, varying structure of bursts from this source, we report best-fit parameters using models that do not explicitly fit for one-sided scattering tails, and thus yield estimates of “observed” widths. Best-fit observed widths and burst arrival times, referenced to the Solar System Barycentre and infinite frequency using per-burst DMs and the EVN position¹⁰ for this source are presented in Extended Data Table 1.

Two CHIME/FRB events from FRB 180916.J0158+65 (on MJDs 58392 and 58720) consist of two sub-bursts that occur widely separated in time, with no emission observed between them. In such cases it is unclear whether these pairs of bursts belong to the same envelope emitted by the source, or if they instead represent distinct moments of source activity. Given this ambiguity, we here consider them to be separate bursts. One

¹https://github.com/danielemichilli/DM_phase

of the events is reported before⁴. Therefore, while we report on 10 events registered by the CHIME/FRB instrument previously⁴, we report values for 11 bursts in Extended Data Table 1.

The burst flux calibration method is nearly identical to that previously presented⁴, with one crucial difference. Previously we assumed that each burst was detected along the meridian of the primary beam, at the peak sensitivity of its declination arc. Under this assumption, we calibrated using meridian transit observations of bright sources near the declination of each burst to obtain lower-bound fluences and fluxes. For the current analysis, we instead leverage the precise localization¹⁰ of FRB 180916.J0158.6 combined with our beam model to scale the fluences and fluxes and obtain more accurate values. From the beam model, we determine a per-frequency scaling between the location of the calibrator at the time of transit and the location of the FRB at the time of burst occurrence. We apply this scaling to the calibrated dynamic spectrum of each burst before generating the band-averaged time series from which the fluence and flux are calculated. If there were multiple sub-bursts in a given burst, then separate fluences and fluxes were obtained for each component.

We use this method to calculate fluences and peak fluxes for all FRB 180916.J0158.6 bursts detected by CHIME/FRB, including recalculations for the ten previously published bursts⁴. More specifically, for each burst located within the FWHM (at 600 MHz) of the synthesized beam in which it was detected, we complete the scaling analysis using the precise position. For all other bursts, we use the method previously presented⁴ to obtain lower bounds. For each calculation, we use meridian transit observations of the supernova remnant SNR G130.7+03.1, which is located within 1° in declination from FRB 180916.J0158.6. Fluences and peak fluxes for all bursts are listed in Extended Data Table 1. For bursts within the beam FWHM, fluences calculated using the precise position are on average $\sim 40\%$ larger than the corresponding lower bounds calculated assuming detection along the meridian.

Including both newly and previously detected bursts, but omitting those for which only lower bounds could be calculated, we obtain a population of fluences for 19 FRB 180916.J0158.6 bursts, or a total of 26 sub-bursts. The cumulative distribution function of the 26 sub-burst fluences ($N(> F) \propto F^{\alpha+1}$ where N is the number of bursts detected above a fluence of F) is shown in Extended Data Figure 3. We determine the power-law index, α , of the differential distribution ($dN/dF \propto F^\alpha$) using maximum-likelihood estimation methods^{44,45}. The turnover in the distribution at lower fluences could be due to our telescope sensitivity limit or the intrinsic burst distribution. To remain agnostic about the cause of the turnover, we pick a fluence threshold that minimizes the Kolmogorov-Smirnov distance between an estimated power law and the underlying distribution. The resulting 6.4 Jy ms threshold is shown in Extended Data Figure 3 as a black dashed vertical line, while our 5.0 Jy ms active period 90% confidence completeness threshold is shown as a blue dash-dotted line. Excluding bursts below the Kolmogorov-Smirnov threshold, we complete a Monte Carlo simulation which resamples the fluences according to their uncertainties to obtain a distribution of estimated power law indices determined

using a maximum-likelihood estimator at each resampling. The mean of the resulting distribution is $\alpha = -2.5 \pm 0.4 \pm 0.1$, where the first error is the statistical uncertainty from the maximum-likelihood estimator and the second error is the standard deviation of the index distribution.

This value is consistent with previous results⁷, which found that the cumulative distribution of energies from FRB 121102 bursts detected at 1.4 GHz using Arecibo followed a power law with $\gamma = -1.8 \pm 0.3$ (equivalent to a differential distribution index of $\alpha = \gamma - 1 = -2.8$). Both of these values are steeper than the $\alpha \sim -1.7$ determined using separate samples of FRB 121102 bursts detected by the Very Large Array at 3 GHz, the Green Bank Telescope at 2 GHz, and Arecibo at 1.4 GHz⁴⁶.

Although the comparison of these values is potentially interesting, we reiterate that all are almost certainly contaminated by instrumental biases and likely do not faithfully reflect the underlying source distributions. More robust conclusions about the intrinsic source luminosity function must wait until our CHIME/FRB detection biases are properly evaluated.

Significance of the period To search for the period, we fold the burst arrival times with different periods, and group the folded bursts into n phase bins¹¹. The folding and grouping of the arrival times make the search relatively insensitive to randomly occurring gaps in the data as long as the exposure is reasonably uniform across phase bins. We then perform the classic Pearson χ^2 test for deviation from uniformity:

$$\chi^2 = \sum_{i=1}^n \frac{(N_i - E_i)^2}{E_i}, \quad (1)$$

where n is the total number of phase bins, N_i is the observed number of bursts in bin i , $E_i = pT_i$ is the expected number of bursts from a uniform distribution, T_i the exposure time for bin i , and $p = \sum N_i / \sum T_i$ the average burst rate per unit exposure time. In the case of uniformity, the calculated χ^2 statistic for different folding periods should follow a chi-squared distribution with $n - 1$ degrees of freedom (DOF) in the limit as $N \rightarrow \infty$. A reduced $\chi^2 \gg 1$ indicates a periodicity unlikely to arise by chance. Note that this χ^2 test, as well as similar tests, implicitly assumes (1) the arrival time of each burst is independent; (2) the number of bursts in each bin follows a Gaussian distribution. Both of the assumptions may fail in the study of FRB arrival times, where the sample size is small, and the arrival of bursts could be non-Poisson. Therefore, after the search, we have applied several approaches to verify the significance.

We searched for periods from $P_{\min} = 1.57$ days to $P_{\max} = 62.8$ days in steps of $0.1/T$ in frequency (i.e. inverse of the period) space, where $T = 408$ days is the longest separation between burst arrival times. We currently only search for periods of days, as opposed to smaller time scales, to avoid the complexity introduced by the cadence of the source transiting CHIME at a sidereal day and CHIME’s beam response during the daily exposure. Moreover, the number of independent periods that need to be searched is proportional to $1/P$, so the “look elsewhere” effect would be orders of magnitude larger for

searches with short periodicity, leading to periodicities arising by chance. P_{\min} is chosen to be sufficiently larger than a sidereal day such that the modulation of the Fourier spectrum from the sidereal day fades away. P_{\max} is chosen so that the extent of the observation time consists of enough cycles. The numbers are chosen to be integer multiples of the irrational number π to avoid integer multiples of the sidereal day, which will lead to uneven exposure across the phase bins.

After calculating the χ^2 against folding period, we noticed a distinct peak at $P = 16.35 \pm 0.18$ days, whose reduced $\chi^2 = 15$ with 8 phase bins (7 DOFs). This corresponds to a probability of chance coincidence of 10^{-17} (equivalent to 8.5σ) after taking into consideration the number of independent trials searched $N_{\text{ind}} = (1/P_{\min} - 1/P_{\max})T \sim 250$. The period uncertainty is conservatively estimated by $\sigma_P = P W_{\text{active}}/T_{\text{span}}$, where P is the period, W_{active} is the active days in the period, and T_{span} is the longest time separation between burst arrival times. It corresponds to a change in period that would allow the folded phase to drift across the active cycle over the observed time span, and the calculated error also corresponds to the FWHM of the peak in the periodogram. Since the total number of bursts is not large enough for perfect Gaussian approximation, we verify this significance with a simple calculation. Given that all the bursts arrive in a 4-day phase window, the chance of 28 bursts all falling into the window is $(4/16.35)^{27}$, which corresponds to 7.5σ after taking into account 250 independent trials searched.

The above analysis shows that there is a significant 16.35-day periodicity in the arrival times of FRB 180916.J0158+65 assuming all the bursts are independent events (Poisson statistics). However, with the first repeater, FRB 121102, where no periodicity has currently been found, the bursts are observed to be clustered¹². This triggers the concern that the arrival times of nearby bursts may not be independent. In order to reduce the influence of clustering on our results, we apply the same search using active days, instead of the individual bursts, by assigning a total weight of unity to bursts that arrived on the same sidereal day, so that they are considered as one independent sample. After weighting, there are 18 active dates, for the 28 bursts detected by CHIME/FRB. In this way, we also reduce the influence from inaccurate mapping of beam response within the exposure of a sidereal day.

After weighting the events, the distinct peak at 16.35 days persists in the χ^2 against folding periods, followed by a peak at its harmonic of ~ 32.7 days. The reduced χ^2 versus period with 8 phase bins is shown in Figure 1a. For a χ^2 distribution of 7 DOF, the corresponding chances of the highest peak is $\sim 10^{-7}$, equivalent to 5σ , taking into consideration the number of independent trials searched. And the chance of 18 independent samples to falling into the 4-day window is $(4/16.35)^{17}$, which corresponds to 5.7σ after considering the 250 trials searched.

Given that the 16.35-day periodicity is not an integer number of sidereal days, the influence of the exposure map on the significance is small. To further exclude the possibility of instrumental periodicity, we applied bootstrap tests to the mock burst arrival times randomly sampled according to the daily exposure to FRB 180916.J0158+65 within the FWHM of the telescopes synthesized beams at 600 MHz, as well as to a random selec-

tion of single bursts from Galactic radio pulsars at similar declinations and detected by CHIME/FRB. An example of the reduced χ^2 versus period from two sets of the random samples with the same number of active days as FRB 180916.J0158+65 is shown in Figure 1b (random sample selected according to the exposure map) and Figure 1c (random samples from the detection of PSR B2319+60). With 10^6 sets of random samples from the exposure map, and 10^6 sets each from PSR B2319+60, B0138+59, B2224+65, we have not found any period, unrelated to sidereal day, as significant as the 16.35-day period for FRB 180916.J0158+65.

For a most conservative case, we assume all the bursts arriving in the active phase of the same cycle are clustered due to mechanisms irrelevant to the periodicity, the chance of 11 cycles of bursts all falling in the 4-day window is still only $(4/16.35)^{10}$, which corresponds to 3.8σ after taking into account 250 independent trials searched. A similar result (3.5 sigma) is obtained by assigning a total weight of units for bursts with separation less than 4 days and searching for periods. The 16.35-day periodicity is still the most prominent peak with this approach. Therefore, we conclude that the periodicity is significant even after taking into account potential clustering.

We also performed the H-test summing over 8 harmonics¹³, and Discrete Fourier Transform searches with incoherent harmonic summing¹⁴ on the arrival times of FRB 180916.J0158+65. With all the approaches, with or without subtracting the exposure map, with different weighting, the $\sim 16.35 \pm 0.18$ day period remains prominent, and the significance varies between 4–11 σ . No other statistically significant periods (other than those harmonically related to this ~ 16 day-period) appear in the searched range.

Although the definite value of the significance of the observed periodicity is undetermined due to our incomplete knowledge of the underlying burst distribution, the periodicity is obvious with all the approaches we have tried, and does not exist in any of the control samples. Therefore, we conclude that the periodicity of FRB 180916.J0158+65 is significant and astrophysical in origin.

Exposure & Fluence Completeness Determination The exposure to the EVN position¹⁰ for the source was calculated by adding up the duration of daily transits across the FWHM region of the synthesized beams of the CHIME/FRB system at 600 MHz. After excluding transits for which the observations were interrupted by pipeline upgrades and testing, we estimate the total exposure to be 64 hours in the interval from 2018 August 28 to 2019 September 30. We report exposure up to 2019 September 30 since several upgrades were made to the CHIME/FRB detection pipeline through 2019 October making characterization of the exposure and sensitivity variation difficult. The increased exposure time for several days in 2019 February is due to occurrence of two transits in the same UTC day caused by the differing lengths of a solar and a sidereal day (see Figure 2).

Since the burst activity is not constant within the active phase (see Figure 3c), we derive two estimates of the exposure and detection rate for the active phases of the source. These estimates assume different durations of the active phase, one being the standard deviation in the phases derived by folding burst arrival times at the 16.35-day period

(± 0.8 -day interval) and the other being a ± 2.6 -day interval which includes the arrival times of all bursts.

A total of 7 hours of the exposure was within a ± 0.8 -day interval of estimated epochs of source activity, with 12 out of the 28 reported bursts detected in this period. The other 16 bursts were not included in the calculation of the detection rate for various reasons. Seven of these bursts were emitted outside the fiducial definition of the active phase, two of these bursts were detected in October 2019 (after the interval used for the evaluation of the exposure), six were detected when the source location was not within the FWHM region of the synthesized beams at 600 MHz and one was detected on 2018 September 16 when system metrics were not being recorded by the detection pipeline.

The CHIME/FRB system was operating nominally for a total of 20 hours in the active phases defined as a ± 2.6 -day interval around each epoch of source activity. Nineteen of the 28 detections occurred during intervals included in this exposure time, with seven bursts which were excluded from the previous definition of the active phase being included here. The exposure in the inactive phase (outside the ± 2.6 -day intervals around the estimated epochs of activity for the source) was a total of 44 hours.

In order to characterize the variation in sensitivity (due to changes in gain calibration, the detection pipeline and RFI environment) for each day included in the exposure, we use a method described previously¹⁶. We analyze the distribution of S/Ns of pulsars detected with the CHIME/FRB system within 10° of the source declination. In contrast to the approach used previously¹⁶, we use pulsars which were detected on each sidereal day for which the telescope was operating with the same gain calibration, instead of within a UTC day. For each pulsar, the rms noise is measured relative to the median over all days the pulsar was detected. A weighted average of these measurements for all pulsars provides an estimate of the overall variation in rms noise on each sidereal day.

Fluence completeness was determined following previously reported methods^{4,16}. We use the bursts reported in Extended Data Table 1 to simulate fluence thresholds for both the active and inactive periods, finding completeness at the 90% confidence interval of 5.2 Jy ms and 5.1 Jy ms, respectively.

Effelsberg observations and analysis Motivated by the detection of the 16.35-day period, we observed FRB 180916.J0158+65 at 1.4 GHz using the 100-m Effelsberg radio telescope and PSRIX data recorder⁴⁷ for 17.6 hr during a predicted active period (2019 October 29 and 2019 October 30). Details of the scan start times and durations are shown in Extended Data Table 2. We observed with a total bandwidth of 250 MHz, from 1234 MHz to 1484 MHz, divided into 2048 channels. The data were recorded with a time and frequency resolution of 131.072 μ s and 0.122 MHz, respectively.

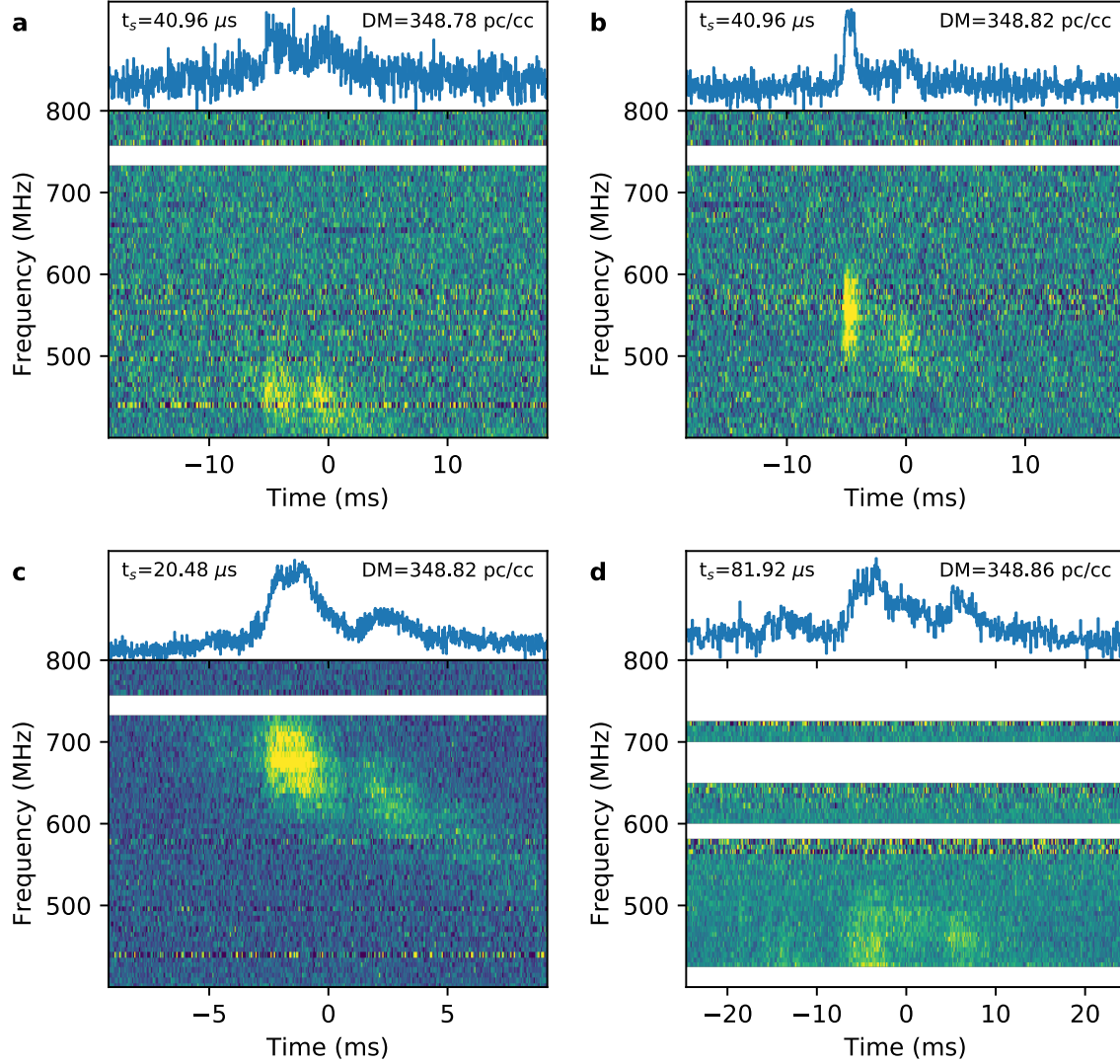
The high-time resolution data were analyzed in the search for millisecond-duration radio bursts, using tools from the PRESTO suite of pulsar software⁴⁸. The data were first searched for radio frequency interference (RFI), and the contaminated frequency channels and time intervals were masked using the tool `rfifind`. Dedispersed time series were generated for the DM range 300–400 pc cm⁻³ in DM steps of 0.3 pc cm⁻³ using

the tool `prepdata`. We searched each dedispersed time series for single pulses using `single_pulse_search.py`. The single pulses identified were filtered for RFI in the search for astrophysical bursts, above a 7σ threshold, using an automated classifier^{49,50}. Given the frequency resolution of the PSRIX data, the intra-channel smearing is ~ 0.15 ms at the DM of FRB 180916.J0158+65. This is comparable to the time resolution of the data. Our search was sensitive up to burst widths of 39.3 ms. Bursts from FRB 180916.J0158+65 have been observed with components as narrow as $\sim 60 \mu\text{s}$ ¹⁰. Therefore, it is possible that FRB 180916.J0158+65 is producing weak, narrow bursts that we were not sensitive to in this search.

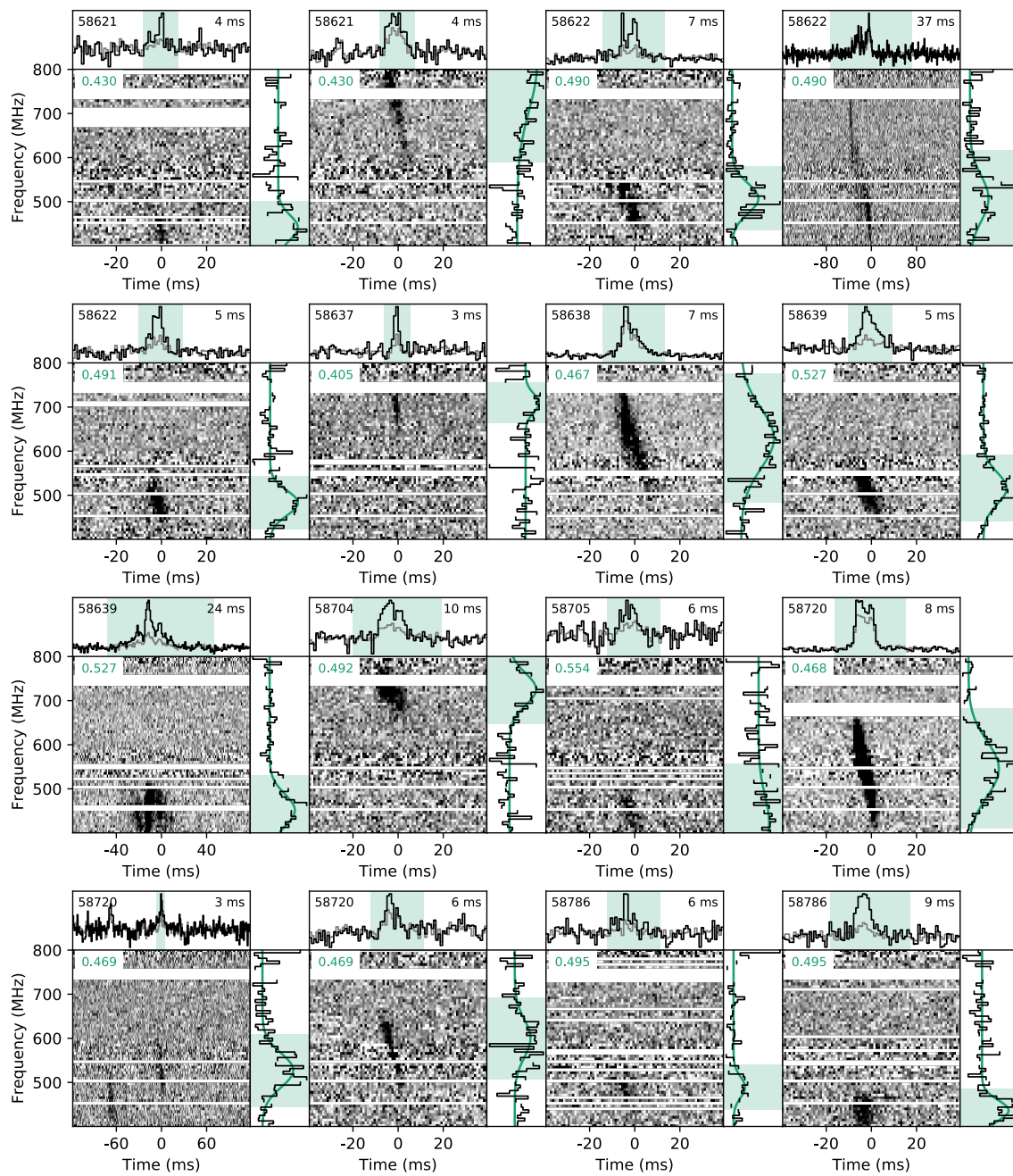
In this search we did not detect any bursts from FRB 180916.J0158+65 above a 7σ threshold. By taking typical values of the system temperature and gain for Effelsberg ($T_{\text{sys}} \approx 20$ K, $G \approx 1.54$ K Jy⁻¹), estimating a background temperature of 5 K using the 408 MHz all-sky map⁵¹ and extrapolating to 1.4 GHz using a spectral index⁵² of -2.7 , we use the radiometer equation to derive the fluence limit of our search (following⁵³). Assuming a burst width of 1 ms, we were sensitive to bursts from FRB 180916.J0158+65 above a fluence threshold of 0.17 Jy ms.

Interestingly, during this predicted active epoch of FRB 180916.J0158+65, two bursts, with a fluence exceeding 2 Jy ms, were detected by CHIME/FRB (Extended Data Table 1). The time of arrival of both bursts are within the same Effelsberg scan indicated in Extended Data Table 2. Given our detection threshold of 0.17 Jy ms, if these bursts were equally bright at 1.4 GHz, our search was sufficiently sensitive to detect them. The spectra of the two CHIME/FRB bursts peak in the lower half of the 400–800 MHz band. The detection of bursts with CHIME/FRB and contemporaneous non-detection with Effelsberg suggests that observed activity from FRB 180916.J0158+65 depends on frequency. In addition, the previously detected bursts from FRB 180916.J0158+65 with the EVN at 1.7 GHz are found at the leading edge of the activity cycle observed at 400–800 MHz (Figure 3). Future multi-frequency observations of FRB 180916.J0158+65 during predicted active periods are crucial in order to quantify this behaviour.

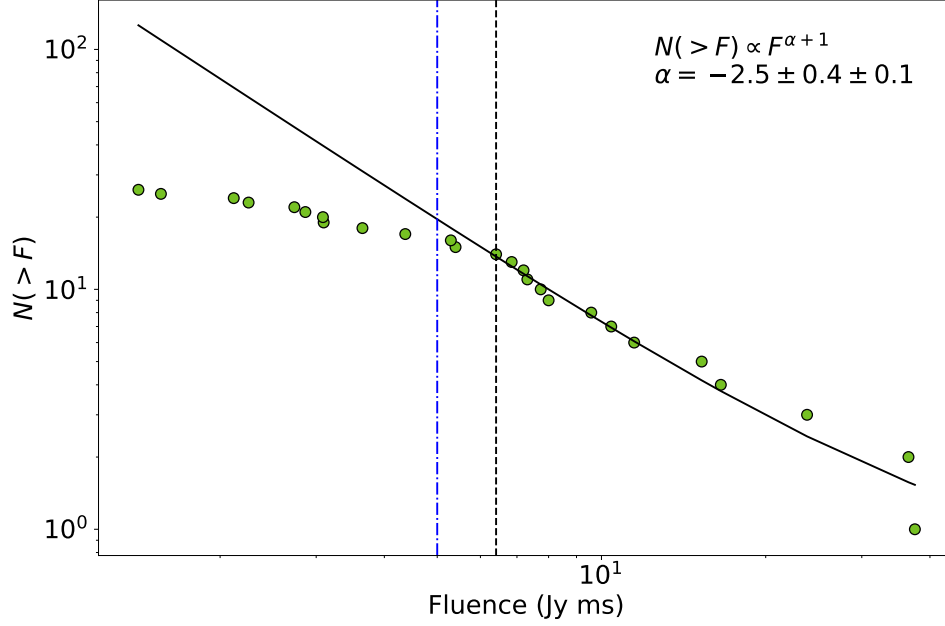
Extended Data



Extended Data Figure 1: **Dynamic spectra of bursts with available baseband data.** The 181225 (a), 181226 (b), 190604 (c) and 190605 (d) bursts, dedispersed to the per-burst optimal DMs that are listed in the top right corner of each panel. The sampling time after downsampling is listed in the top left corner of each panel. Intensity values are saturated at the 1st and 99th percentiles. 64 frequency subbands with a 6.25 MHz subband bandwidth are shown for all bursts. Horizontal white bands represent missing or masked data.



Extended Data Figure 2: **Dynamic spectra of 17 newly reported bursts.** All bursts are dedispersed to $348.82 \text{ pc cm}^{-3}$. The arrival phase of the bursts within the 16.35-day cycle is written in the top left corner. Every panel shows the 0.98304-ms time resolution dedispersed intensity data with the integrated burst profile on top and the on-pulse spectrum on the right. Intensity values are saturated at the 5th and 95th percentiles. Pulse widths, defined as the width of the boxcar with the highest S/N after convolution with the burst profile, are in the top-right corner. The shaded region in the profile (four times the pulse width) was used for the extraction of the on-pulse spectrum. The shaded region in the on-pulse spectrum shows the full width at tenth maximum (FWTM) of a Gaussian fit. In the burst profiles, the black lines are the integration over the FWTMs and the gray lines are the integration over the full bandwidths. For better visualization we downsampled the full-resolution data (16,384 channels) to 64 subbands with 6.25 MHz of bandwidth each. Horizontal white bands represent missing or masked data. There are underlying missing or masked channels at full resolution, resulting in an average effective bandwidth of 224 MHz.



Extended Data Figure 3: **Cumulative distribution of burst fluences.** The distribution is composed of both new bursts and those previously detected⁴. Excluding bursts detected beyond the 600 MHz FWHM of any CHIME/FRB synthesized beam, this includes 19 bursts split into sub-bursts, yielding 26 fluence measurements. The black solid line represents the maximum-likelihood estimated power law with differential distribution index $\alpha = -2.5 \pm 0.4 \pm 0.1$, where the first error is the statistical uncertainty from the maximum-likelihood estimator and the second error is the standard deviation of the distribution of power-law indices obtained from a Monte Carlo simulation that resamples the fluences according to their uncertainties. The black dashed vertical line denotes the 6.4 Jy ms threshold determined by minimizing the Kolmogorov-Smirnov distance between a power-law fit and the underlying data. The blue dash-dotted vertical line denotes the 5.0 Jy ms active period 90% confidence completeness threshold.

[hbp]

Extended Data Table 1: **Burst Properties.** Best-fit parameters for 28 bursts from FRB 180916.J0158+65 detected by CHIME/FRB. Uncertainties are reported at the 68.3% confidence level. Bursts with multiple components have one arrival time and several widths, fluences, and peak fluxes reported; the arrival time refers to the arrival of the first sub-burst from the EVN position at the Solar System Barycentre after correcting to infinite frequency (i.e., after removing the time delay from dispersion) using the listed DM. Fluence and peak flux values for each sub-burst component are presented in order of arrival.

MJD	DM (pc cm ⁻³)	Total Width (ms)	Fluence (Jy ms)	Peak Flux (Jy)
Previously Published Bursts ⁴				
58377.42972096	349.2±0.2	1.40±0.07	>2.3±1.2	>1.4±0.6
58410.34656422 ^a	349.0±0.6	4.1±0.3	>3.5±1.3	>0.6±0.3
58410.34656495 ^a	349.0±0.6	4.4±0.9	>2.0±0.8	>0.3±0.2
58426.29413444	349.5±0.3	1.37±0.07	>2.8±0.9	>1.4±0.5
58426.30088378	349.6±0.2 ^b	6.3±1.1	6.8±3.0	1.0±0.6
58442.25174905	349.9±0.6	1.10±0.09	8.0±2.2	2.9±1.1
58474.17007574	349.1±0.1	4.95±0.4 / 1.51±0.3 / 3.7±0.3 / 2.8±0.3	9.6±2.6 / 15±4 / 16.5±4.5 / 7.2±1.8	1.9±0.6 / 6.3±1.8 / 3.5±1.0 / 0.9±0.4
58475.16454902	349.7±0.7	1.67±0.05 / 6.3±0.4	10.4±2.9 / 3.6±1.5	1.9±0.6 / 0.5±0.3
58477.16557196	348.9±0.7	3.8±0.3	3.1±2.4	1.4±0.8
58478.15889115	348.8±0.8	0.87±0.3 / 3.6±0.4	2.9±0.8 / 1.6±0.5	1.9±0.6 / 0.7±0.3
58509.06654412	349.8±0.5	2.53±0.13	6.4±1.2	1.7±0.5
Bursts from This Work				
58621.75641235	349.8±0.7 ^b	2.5±0.6	1.0±0.3	0.4±0.2
58621.76154355	350.2±0.3	1.96±0.16	7.7±1.8	1.6±0.5
58622.74024356	348.9±0.1	0.58±0.08 / 0.9±0.1	>1.3±0.5 / >2.2±0.9	>0.8±0.4 / >0.8±0.5
58622.75315853	349.4±0.2	8.0±0.7 / 2.63±0.16	3.1±1.4 / 5.3±2.4	0.9±0.5 / 1.0±0.6
58622.75441645	349.3±0.4	3.6±0.4	4.4±2.0	1.1±0.7
58637.71187752	349.9±0.5	1.9±0.2	2.1±0.8	1.6±0.8
58638.71347350	348.82±0.05 ^c	1.00±0.05	37±9	6.3±1.9
58639.70267121	349.7±0.2	2.34±0.08	>7.0±1.5	>1.3±0.4
58639.70713864	348.86±0.5 ^c	3.72±0.13 / 4.1±0.4	11.5±4.0 / 5.4±2.7	2.3±0.7 / 1.1±0.5
58704.53530987	349.6±0.3	3.43±0.14	7.3±1.2	1.2±0.3
58705.53461219	349.3±0.9 ^b	4.3±1.6	>1.7±0.3	>0.4±0.2
58720.49302597	349.0±0.1	1.83±0.03	24±4	4.9±1.0
58720.49551788 ^a	349.7±0.4	7.8±1.3	2.8±0.9	0.6±0.3
58720.49551860 ^a	349.7±0.4	5.1±0.8	1.4±0.6	0.5±0.3
58720.49669723	349.5±0.5	1.3±0.3	>2.6±0.5	>0.9±0.3
58786.31947315	349.7±0.7 ^b	3.1±0.7	2.3±0.8	0.9±0.8
58786.32497962	349.1±0.4 ^b	3.6±0.4	>2.3±0.5	>0.5±0.2

^a Considered to be separate bursts observed during the same CHIME/FRB event due to large time separation and no clear emission between bursts. See Methods for a brief discussion.

^b From S/N-optimization.

^c From structure-optimization of CHIME/FRB baseband data.

Extended Data Table 2: **Effelsberg observations.** Details of the observations of FRB 180916.J0158+65 using the 100-m Effelsberg telescope on 29th October 2019 and 30th October 2019.

^a Times quoted at the Solar System Barycentre after correcting to infinite frequency (i.e. after removing the time delay from dispersion) using a DM^{10} of $348.76 \text{ pc cm}^{-3}$.

* Two bursts were detected by CHIME/FRB during this scan.

	Scan time range (date time UTC)	Scan time range ^a (MJD)	Duration (s)
	2019 Oct 29 22:16:20 – 2019 Oct 30 00:16:06	58785.93233 – 58786.01550	7186
	2019 Oct 30 00:18:40 – 2019 Oct 30 02:18:23	58786.01728 – 58786.10043	7183
	2019 Oct 30 02:20:50 – 2019 Oct 30 04:20:39	58786.10212 – 58786.18534	7190
	2019 Oct 30 04:23:10 – 2019 Oct 30 06:22:58	58786.18708 – 58786.27027	7188
*	2019 Oct 30 06:25:30 – 2019 Oct 30 08:25:14	58786.27203 – 58786.35519	7184
	2019 Oct 30 08:39:30 – 2019 Oct 30 10:39:18	58786.36509 – 58786.44829	7188
	2019 Oct 30 10:41:50 – 2019 Oct 30 10:58:53	58786.45005 – 58786.46189	1023
	2019 Oct 30 19:33:40 – 2019 Oct 30 21:33:27	58786.81938 – 58786.90257	7187
	2019 Oct 30 21:36:00 – 2019 Oct 30 23:35:44	58786.90434 – 58786.98749	7184
	2019 Oct 30 23:38:10 – 2019 Oct 31 01:00:04	58786.98918 – 58787.04606	4914

Acknowledgements We thank the Dominion Radio Astrophysical Observatory, operated by the National Research Council Canada, for gracious hospitality and useful expertise. The CHIME/FRB Project is funded by a grant from the Canada Foundation for Innovation 2015 Innovation Fund (Project 33213), as well as by the Provinces of British Columbia and Québec, and by the Dunlap Institute for Astronomy and Astrophysics at the University of Toronto. Additional support was provided by the Canadian Institute for Advanced Research (CIFAR), McGill University and the McGill Space Institute via the Trottier Family Foundation, and the University of British Columbia. The Dunlap Institute is funded by an endowment established by the David Dunlap family and the University of Toronto. Research at Perimeter Institute is supported by the Government of Canada through Industry Canada and by the Province of Ontario through the Ministry of Research & Innovation. The National Radio Astronomy Observatory is a facility of the National Science Foundation (NSF) operated under cooperative agreement by Associated Universities, Inc. FRB research at UBC is supported by an NSERC Discovery Grant and by the Canadian Institute for Advanced Research. The CHIME/FRB baseband system is funded in part by a CFI John R. Evans Leaders Fund grant to I.H.S. The Dunlap Institute is funded through an endowment established by the David Dunlap family and the University of Toronto. The National Radio Astronomy Observatory is a facility of the National Science Foundation operated under cooperative agreement by Associated Universities, Inc. A.S.H. was partly supported by the Dunlap Institute at the University of Toronto. B.M. acknowledges support from the Spanish Ministerio de Economía y Competitividad (MINECO) under grants AYA2016-76012-C3-1-P and MDM-2014-0369 of ICCUB (Unidad de Excelencia “María de Maeztu”). B.M.G. acknowledges the support of the Natural Sciences and Engineering Research Council of Canada (NSERC) through grant RGPIN-2015-05948, and of the Canada Research Chairs program. D.M. is a Banting Fellow. M.B. is supported by an FRQNT Doctoral Research Award. M.D. is supported by a Killam Fellowship and receives support from an NSERC Discovery Grant, the Canadian Institute for Advanced Research (CIFAR), and from the FRQNT Centre de Recherche en Astrophysique du Quebec. P.C. is supported by an FRQNT Doctoral Research Award. P.S. is a Dunlap Fellow and an NSERC Postdoctoral Fellow. S.M.R. is a CIFAR Fellow and is supported by the NSF Physics Frontiers Center award 1430284. U.-L.P. receives support from Ontario Research Fund-Research Excellence Program (ORF-RE), Natural Sciences and Engineering Research Council of Canada (NSERC), Simons Foundation, Thoth Technology Inc, and Alexander von Humboldt Foundation. V.M.K. holds the Lorne Trottier Chair in Astrophysics & Cosmology and a Canada Research Chair and receives support from an NSERC Discovery Grant and Herzberg Award, from an R. Howard Webster Foundation Fellowship from the Canadian Institute for Advanced Research (CIFAR), and from the FRQNT Centre de Recherche en Astrophysique du Quebec. Z.P. is supported by a Schulich Graduate Fellowship. F.K. acknowledges support by the Swedish Research Council. The European VLBI Network is a joint facility of independent European, African, Asian, and North American radio astronomy institutes. Scientific results from EVN data presented in this publication are derived from the following EVN project code: EM135. Based in part on observations with the 100-m telescope of the MPIfR (Max-Planck-Institut für Radioastronomie) at Effelsberg. We thank Laura Spitler, Marilyn Cruces and Michael Kramer for their help in acquiring Effelsberg observing time.

Author Contributions All authors from CHIME/FRB collaboration played either leadership or significant supporting roles in one or more of: the management, development and construc-

tion of the CHIME telescope, the CHIME/FRB instrument and the CHIME/FRB software data pipeline, the commissioning and operations of the CHIME/FRB instrument, the data analysis and preparation of this manuscript. All authors from CHIME collaboration played either leadership or significant supporting roles in the management, development and construction of the CHIME telescope. K.N., J.W.T.H., B.M., Z.P., A.K., F.K. and R.K. performed the analysis of EVN and Effelsberg single-dish data presented here.

Competing Interests The authors declare that they have no competing financial interests.

Correspondence Correspondence and requests for materials should be addressed to D. Z. Li (email: dzli@cita.utoronto.ca).
 1. Lorimer, D. R., Bailes, M., McLaughlin, M. A., Narkevic, D. J. & Crawford, F. A Bright Millisecond Radio Burst of Extragalactic Origin. *Science* **318**, 777 (2007). 0709.4301.

2. Spitler, L. G. *et al.* A repeating fast radio burst. *Nature* **531**, 202–205 (2016). 1603.00581.
3. CHIME/FRB Collaboration *et al.* A second source of repeating fast radio bursts. *Nature* **566**, 235–238 (2019).
4. CHIME/FRB Collaboration *et al.* CHIME/FRB Detection of Eight New Repeating Fast Radio Burst Sources. *Astrophys. J. Letters* **885**, L24 (2019). 1908.03507.
5. Scholz, P. *et al.* The Repeating Fast Radio Burst FRB 121102: Multi-wavelength Observations and Additional Bursts. *Astrophys. J.* **833**, 177 (2016). 1603.08880.
6. Zhang, Y. G. *et al.* Fast Radio Burst 121102 Pulse Detection and Periodicity: A Machine Learning Approach. *Astrophys. J.* **866**, 149 (2018). 1809.03043.
7. Gourdji, K. *et al.* A Sample of Low-energy Bursts from FRB 121102. *Astrophys. J. Letters* **877**, L19 (2019). 1903.02249.
8. Oppermann, N., Yu, H.-R. & Pen, U.-L. On the non-Poissonian repetition pattern of FRB121102. *Mon. Not. R. Astron. Soc.* **475**, 5109–5115 (2018). 1705.04881.
9. CHIME/FRB Collaboration *et al.* The CHIME Fast Radio Burst Project: System Overview. *Astrophys. J.* **863**, 48 (2018). 1803.11235.
10. Marcote, B. *et al.* A repeating fast radio burst source localized to a nearby spiral galaxy. *Nature* **577**, 190–194 (2020).
11. Leahy, D. A. *et al.* On searches for pulsed emission with application to four globular cluster X-ray sources : NGC 1851, 6441, 6624 and 6712. *Astrophys. J.* **266**, 160–170 (1983).

12. Oppermann, N., Yu, H.-R. & Pen, U.-L. On the non-Poissonian repetition pattern of FRB121102. *Mon. Not. R. Astron. Soc.* **475**, 5109–5115 (2018). 1705.04881.
13. de Jager, O. C., Raubenheimer, B. C. & Swanepoel, J. W. H. A powerful test for weak periodic signals with unknown light curve shape in sparse data. *Astron. & Astrophys.* **221**, 180–190 (1989).
14. Ransom, S. M., Eikenberry, S. S. & Middleditch, J. Fourier techniques for very long astrophysical time-series analysis. *Astron. J.* **124**, 1788–1809 (2002).
15. Hessels, J. W. T. *et al.* FRB 121102 Bursts Show Complex Time-Frequency Structure. *Astrophys. J. Letters* **876**, L23 (2019). 1811.10748.
16. Josephy, A. *et al.* CHIME/FRB Detection of the Original Repeating Fast Radio Burst Source FRB 121102. *arXiv e-prints* arXiv:1906.11305 (2019). 1906.11305.
17. Ord, S. M., Bailes, M. & van Straten, W. The Scintillation Velocity of the Relativistic Binary Pulsar PSR J1141-6545. *Astrophys. J. Letters* **574**, L75–L78 (2002). astro-ph/0204421.
18. Rickett, B. J. *et al.* Interstellar Scintillation of the Double Pulsar J0737-3039. *Astrophys. J.* **787**, 161 (2014). 1404.1120.
19. Reardon, D. J. *et al.* Modelling annual and orbital variations in the scintillation of the relativistic binary PSR J1141-6545. *Mon. Not. R. Astron. Soc.* **485**, 4389–4403 (2019). 1903.01990.
20. Fruchter, A. S., Stinebring, D. R. & Taylor, J. H. A millisecond pulsar in an eclipsing binary. *Nature* **333**, 237–239 (1988).
21. Johnston, S. *et al.* PSR 1259–63: A binary radio pulsar with a Be star companion. *Astrophys. J. Letters* **387**, L37–L41 (1992).
22. Kaspi, V. M. *et al.* A massive radio pulsar binary in the Small Magellanic Cloud. *Astrophys. J. Letters* **423**, L43–L45 (1994).
23. Stairs, I. H. *et al.* PSR J1740–3052— a pulsar with a massive companion. *Mon. Not. R. Astron. Soc.* **325**, 979–988 (2001).
24. Chernyakova, M. *et al.* Multi-wavelength observations of the binary system PSR B1259-63/LS 2883 around the 2014 periastron passage. *Mon. Not. R. Astron. Soc.* **454**, 1358–1370 (2015). 1508.01339.
25. Mottez, F. & Zarka, P. Radio emissions from pulsar companions: a refutable explanation for galactic transients and fast radio bursts. *Astron. & Astrophys.* **569**, A86 (2014). 1408.1333.

26. Zhang, B. Frb 121102: A repeatedly combed neutron star by a nearby low-luminosity accreting supermassive black hole. *The Astrophysical Journal Letters* **854**, L21 (2018).
27. Thorne, K. S., Price, R. H. & MacDonald, D. A. *Black holes: The membrane paradigm* (1986).
28. Main, R. *et al.* Pulsar emission amplified and resolved by plasma lensing in an eclipsing binary. *Nature* **557**, 522–525 (2018). 1805.09348.
29. Bilous, A. V., Ransom, S. M. & Demorest, P. Unusually Bright Single Pulses from the Binary Pulsar B1744-24A: A Case of Strong Lensing? *Astrophys. J.* **877**, 125 (2019). 1811.05766.
30. Feldbrugge, J., Pen, U.-L. & Turok, N. Oscillatory path integrals for radio astronomy. *arXiv e-prints* arXiv:1909.04632 (2019). 1909.04632.
31. Lyubarsky, Y. A model for fast extragalactic radio bursts. *Mon. Not. R. Astron. Soc.* **442**, L9–L13 (2014). 1401.6674.
32. Beloborodov, A. M. A Flaring Magnetar in FRB 121102? *Astrophys. J. Letters* **843**, L26 (2017). 1702.08644.
33. Metzger, B. D., Margalit, B. & Sironi, L. Fast radio bursts as synchrotron maser emission from decelerating relativistic blast waves. *arXiv preprint arXiv:1902.01866* (2019).
34. Olausen, S. A. & Kaspi, V. M. The McGill Magnetar Catalog. *ApJS* **212**, 6 (2014).
35. D’Ài, A. *et al.* Evidence for the magnetar nature of 1E 161348-5055 in RCW 103. *Mon. Not. R. Astron. Soc.* **463**, 2394–2404 (2016).
36. Tendulkar, S. P., Kaspi, V. M., Archibald, R. F. & Scholz, P. A Near-infrared Counterpart of 2E1613.5-5053: The Central Source in Supernova Remnant RCW103. *Astrophys. J.* **841**, 11 (2017). 1610.02268.
37. Xu, K. & Li, X.-D. On the Fallback Disk around the Slowest Isolated Pulsar, 1E 161348-5055. *Astrophys. J.* **877**, 138 (2019).
38. Kramer, M., Lyne, A. G., O’Brien, J. T., Jordan, C. A. & Lorimer, D. R. A Periodically Active Pulsar Giving Insight into Magnetospheric Physics. *Science* **312**, 549–551 (2006). astro-ph/0604605.
39. Shaham, J. Free precession of neutron stars: role of possible vortex pinning. *Astrophys. J.* **214**, 251–260 (1977).

40. Sedrakian, A., Wasserman, I. & Cordes, J. M. Precession of isolated neutron stars. I. Effects of imperfect pinning. *Astrophys. J.* **524**, 341–460 (1999).
41. Akgün, T., Link, B. & Wasserman, I. Precession of the isolated neutron star PSR B1828-11. *Mon. Not. R. Astron. Soc.* **365**, 653–672 (2006). [astro-ph/0506606](#).
42. Goglichidze, O. A. & Barsukov, D. P. A possible way to reconcile long-period precession with vortex pinning in neutron stars. *Mon. Not. R. Astron. Soc.* **482**, 3032–3044 (2019). [1901.01547](#).
43. CHIME/FRB Collaboration *et al.* Observations of fast radio bursts at frequencies down to 400 megahertz. *Nature* **566**, 230–234 (2019). [1901.04524](#).
44. Clauset, A., Shalizi, C. R. & Newman, M. E. J. Power-Law Distributions in Empirical Data. *SIAM Review* **51**, 661–703 (2009).
45. Alstott, J., Bullmore, E. & Plenz, D. powerlaw: A Python Package for Analysis of Heavy-Tailed Distributions. *PLoS ONE* **9**, e85777 (2014). [1305.0215](#).
46. Law, C. J. *et al.* A Multi-telescope Campaign on FRB 121102: Implications for the FRB Population. *Astrophys. J.* **850**, 76 (2017).
47. Lazarus, P. *et al.* Prospects for high-precision pulsar timing with the new Effelsberg PSRIX backend. *Mon. Not. R. Astron. Soc.* **458**, 868–880 (2016). [1601.06194](#).
48. Ransom, S. M. *New search techniques for binary pulsars*. Ph.D. thesis, Harvard University (2001).
49. Michilli, D. *et al.* Single-pulse classifier for the LOFAR Tied-Array All-sky Survey. *Mon. Not. R. Astron. Soc.* **480**, 3457–3467 (2018). [1808.05424](#).
50. Michilli, D. & Hessels, J. W. T. SpS: Single-pulse Searcher (2018). [1806.013](#).
51. Remazeilles, M., Dickinson, C., Banday, A. J., Bigot-Sazy, M. A. & Ghosh, T. An improved source-subtracted and destriped 408-MHz all-sky map. *Mon. Not. R. Astron. Soc.* **451**, 4311–4327 (2015). [1411.3628](#).
52. Reich, P. & Reich, W. A map of spectral indices of the galactic radio continuum emission between 408 MHz and 1420 MHz for the entire northern sky. *Astron. & Astrophys. Suppl. Ser.* **74**, 7–23 (1988).
53. Cordes, J. M. & McLaughlin, M. A. Searches for Fast Radio Transients. *Astrophys. J.* **596**, 1142–1154 (2003). [astro-ph/0304364](#).